A&A 675, A71 (2023)
https://doi.org/10.1051/0004-6361/202245455

Astronomy & Astrophysics

Probable brown dwarf companions detected in binary microlensing events during the 2018–2020 seasons of the KMTNet survey

Cheongho Han[1], Youn Kil Jung[2], Doeon Kim[1], Andrew Gould[3,4], Valerio Bozza[5,6], Ian A. Bond[7], Sun-Ju Chung[2], Michael D. Albrow[8], Kyu-Ha Hwang[2], Yoon-Hyun Ryu[2], In-Gu Shin[9], Yossi Shvartzvald[10], Hongjing Yang[11], Weicheng Zang[9,11], Sang-Mok Cha[2,12], Dong-Jin Kim[2], Hyoun-Woo Kim[2], Seung-Lee Kim[2], Chung-Uk Lee[2], Dong-Joo Lee[2], Jennifer C. Yee[9], Yongseok Lee[2,13], Byeong-Gon Park[2,13], Richard W. Pogge[4], (The KMTNet Collaboration)
Fumio Abe[14], Richard Barry[15], David P. Bennett[15,16], Aparna Bhattacharya[15,16], Hirosame Fujii[14], Akihiko Fukui[17,18], Yuki Hirao[19], Stela Ishitani Silva[16,20], Rintaro Kirikawa[19], Iona Kondo[19], Naoki Koshimoto[21], Yutaka Matsubara[14], Sho Matsumoto[19], Shota Miyazaki[19], Yasushi Muraki[14], Arisa Okamura[19], Greg Olmschenk[16], Clément Ranc[22], Nicholas J. Rattenbury[23], Yuki Satoh[19], Takahiro Sumi[19], Daisuke Suzuki[19], Taiga Toda[19], Paul J. Tristram[24], Aikaterini Vandorou[15,16], Hibiki Yama[19], and Yoshitaka Itow[14], (The MOA Collaboration)

(Affiliations can be found after the references)

Received 14 November 2022 / Accepted 9 May 2023

ABSTRACT

Aims. We inspect the microlensing data of the KMTNet survey collected during the 2018–2020 seasons in order to find lensing events produced by binaries with brown dwarf (BD) companions.
Methods. In order to pick out binary-lens events with candidate BD lens companions, we conducted systematic analyses of all anomalous lensing events observed during the seasons from 2018 to 2020. By applying a selection criterion of mass ratio between the lens components of $0.03 \lesssim q \lesssim 0.1$, we identify four binary-lens events with candidate BD companions, namely KMT-2018-BLG-0321, KMT-2018-BLG-0885, KMT-2019-BLG-0297, and KMT-2019-BLG-0335. For the individual events, we present interpretations of the lens systems and measure the observables that can be used to constrain the physical lens parameters.
Results. The masses of the lens companions estimated from the Bayesian analyses based on the measured observables indicate high probabilities that the lens companions are in the BD mass regime; that is, 59%, 68%, 66%, and 66% for the four respective events.

Key words. gravitational lensing: micro – brown dwarfs

1. Introduction

As microlensing occurs due to the mass of the foreground object and regardless of its luminosity, it provides an important tool for detecting very faint and even dark astronomical objects. Thanks to this trait, microlensing has been successfully applied to search for extrasolar planets, and about 30 planets all together are detected annually (Gould et al. 2022; Jung et al. 2022; Gould 2022) by surveys such as the KMTNet (Kim et al. 2016), MOA (Bond et al. 2001), and OGLE (Udalski et al. 2015) experiments, with follow-up surveys, such as the ROME/REA survey (Tsapras et al. 2019).

Brown dwarfs (BDs) are another population of faint astronomical objects to which microlensing is sensitive. Microlensing BDs can be detected through a single-lens event channel, in which a single BD object produces a lensing event with a short timescale; for example, Han et al. (2020). Considering that BDs may have formed via a similar mechanism to that of stars, BDs can be as abundant as their stellar siblings, and therefore a significant fraction of short-timescale lensing events being detected by the surveys may be produced by BDs. Observationally, both radial-velocity (Grether & Lineweaver 2006) and microlensing (Shvartzvald et al. 2016) studies indicate a deficit of BD companions compared to both stars and planets, suggesting that microlensing may allow us to study the formation mechanism that can lead to stars, BDs, and planets. However, confirming the BD lens nature of a short-timescale event by measuring the mass of the lens is difficult because the event timescale depends not only on the lens mass but also on the distance to the lens and the relative lens–source proper motion. The lens mass can be determined by simultaneously measuring the extra lensing observables of the angular Einstein radius $\theta_{\rm E}$ and microlens parallax $\pi_{\rm E}$, as was achieved for OGLE-2017-BLG-0896 (Shvartzvald et al. 2019), but the fraction of these events is small.

Han et al. (2022, hereafter Paper I), investigated the microlensing survey data collected during the early phase of the KMTNet experiment with the aim of finding microlensing binaries containing BD companions. The strategy applied in Paper I in order to find BD events was to pick out lensing events

produced by binaries with small companion-to-primary mass ratios q; for example, $0.03 \lesssim q \lesssim 0.1$. Considering that typical Galactic lensing events are produced by low-mass stars (Han & Gould 2003), the companions to the lenses of these events are very likely to be BDs.

Following the work done in Paper I, we report four additional BD binary-lensing events found from the systematic investigation of data from the KMTNet survey from seasons between 2018 and 2020. In the interest of future statistical analyses of the properties of BDs based on a uniform sample, we consistently apply the same selection criterion as that applied in Paper I in the selection of BD events.

Our discovery and analysis of the BD events are presented as follows. In Sect. 2, we describe the procedure used to select BD binary-lens events and explain the observations conducted for the selected events. We describe the analysis procedure commonly applied to the lensing events in Sect. 3, and detailed analyses of the individual events are presented in the following subsections. In Sect. 4, we characterize the source stars of the events and estimate the angular Einstein radii of the individual events. In Sect. 5, we estimate the physical parameters of the lens systems by conducting Bayesian analyses of the events using the measured observables of the individual events. A summary of the results found from the analyses and our conclusions are presented in Sect. 6.

2. Event selection and observations

The KMTNet group began conducting a microlensing survey in 2016, observing stars lying toward the dense Galactic bulge field with the use of three telescopes that are globally distributed in the Southern Hemisphere. For the searches of binary lenses possessing BD companions, we inspect the microlensing data acquired by the KMTNet survey during the three seasons from 2018 to 2020. The survey in the 2020 season was only partially conducted because two of the KMTNet telescopes were shutdown due to the COVID-19 pandemic for most of that season.

We selected binary lensing (2L1S) events with candidate BD lens companions by conducting systematic analyses of all anomalous lensing events observed during the three mentioned seasons. Anomalies induced by planetary companions to the lenses, with companion-to-primary mass ratios of the order of 10^{-3} or less, can in most cases be readily identified from the characteristic short-term nature of the anomalies (Gould & Loeb 1992). However, anomalies induced by BD companions, with mass ratios of the order of 10^{-2} usually cannot be treated as perturbations, and therefore it is generally much more difficult to distinguish them from those induced by binary lenses with roughly equal-mass components. We therefore systematically conducted modelings of all anomalous lensing events detected during the seasons, and then selected candidate BD binary-lens events by applying the selection criterion of $q \lesssim 0.1$. The total numbers of lensing events detected by the KMTNet survey are 2781, 3303, and 894 in the 2018, 2019, and 2020 seasons, respectively, and 2L1S events comprise about one-tenth of the total number of events. This fraction of 2L1S events is similar to that found by Shvartzvald et al. (2016) in the OGLE-MOA-Wise sample (12%).

Using this procedure, we identified four 2L1S events with candidate BD companions, including KMT-2018-BLG-0321, KMT-2018-BLG-0885, KMT-2019-BLG-0297, and KMT-2019-BLG-0335. We found no BD event among the events detected in the 2020 season, not only because the number of detected lensing events during the season is relatively small but also because the data coverage of the individual events was sparse due to the use of a single telescope during the great majority of the season. Among these events, KMT-2019-BLG-0297 was additionally observed by the MOA group, who labeled the event as MOA-2019-BLG-131, and we include their data in the analysis. For this event, we use the KMTNet ID reference following the convention of the microlensing community of using the ID reference of the first discovery survey.

The three KMTNet telescopes are identical, with a 1.6 m aperture. The sites of the individual telescopes are the Siding Spring Observatory in Australia (KMTA), the Cerro Tololo Interamerican Observatory in Chile (KMTC), and the South African Astronomical Observatory in South Africa (KMTS). The telescope used for the MOA survey has an aperture of 1.8 m and is located at Mt. John Observatory in New Zealand. The fields of view of the cameras installed on the KMTNet and MOA telescopes are 4 deg^2 and 2.2 deg^2, respectively. Images were primarily taken in the I band for the KMTNet survey and in the customized MOA-R band for the MOA survey. For both surveys, a minor portion of images were acquired in the V band to measure the colors of the source stars. The OGLE survey was conducted during the 2018 and 2019 seasons, but none of the events reported in this work were detected by the OGLE survey.

Reductions of the images and photometry of the events were carried out using the pipelines of the individual survey groups developed by Albrow et al. (2009) for the KMTNet group and Bond et al. (2001) for the MOA group. Following the routine of Yee et al. (2012), we readjust the error bars of each data set estimated by the pipelines so that the error bars are consistent with the scatter of the data and χ^2 per degree of freedom (d.o.f.) for each data set becomes unity. In the process of readjusting error bars, we use the best-fit model after rejecting outliers lying beyond a 3σ level from the best-fit model. The error-bar normalization is an ever-repeating process because once the error bars are rescaled based on a model obtained at a certain stage, the χ^2/d.o.f. value can vary in the next modeling run as the model slightly varies from the initial model, and therefore the value of χ^2/d.o.f. can be slightly different from unity. We note that the variation of the lensing parameters caused by the slight change of the χ^2/d.o.f. value is very minor.

3. Light-curve analyses

Under the approximation of a rectilinear relative motion between the lens and source, the light curve of a 2L1S event is characterized by seven basic lensing parameters. The first three parameters $(t_0, u_0, t_{\rm E})$ define the lens–source approach, and the individual parameters denote the time of the closest approach, the separation between the lens and source at that time (impact parameter), and the Einstein timescale. The Einstein timescale is defined as the time required for a source to cross the Einstein radius, that is, $t_{\rm E} = \theta_{\rm E}/\mu$, where μ denotes the relative lens–source proper motion. Another three parameters (s, q, α) define the binary-lens system, and s denotes the projected separation between the lens components with masses M_1 and M_2, $q = M_1/M_2$ is the mass ratio, and α represents the angle between the direction of $\boldsymbol{\mu}$ and the M_1–M_2 axis (source trajectory angle). Here, $\boldsymbol{\mu}$ represents the vector of the relative lens–source proper motion. The parameters u_0 and s are scaled to $\theta_{\rm E}$. The last parameter ρ is defined as the ratio of the angular source radius θ_* to $\theta_{\rm E}$, that is, $\rho = \theta_*/\theta_{\rm E}$ (normalized source radius), and it characterizes the deformation of a lensing light curve by finite-source effects arising when a source crosses or approaches lens caustics.

Caustics represent source positions at which the lensing magnifications of a point source become infinity. Caustics in binary lensing vary depending on the binary parameters s and q, and their topologies are classified into three categories of "close", "intermediate", and "wide" (Schneider & Weiss 1986; Cassan 2008). A close binary induces three sets of caustics, in which one lies near the heavier lens component and the other two sets lie on the opposite side of the lighter lens component. On the other hand, a wide binary induces two sets of caustics, which lie close to the individual lens components. In the intermediate regime, the caustics merge together to form a single large caustic.

In addition to the basic parameters, the detailed modeling of lensing light curves for a fraction of events requires the consideration of higher-order effects caused by the deviation of the relative lens–source motion from rectilinear. There are two main causes of such a deviation: the first is the accelerated motion of an observer caused by the orbital motion of Earth, that is, microlens–parallax effects (Gould 1992), and the second is the orbital motion of the binary lens, and is referred to as a lens–orbital effect; see, for example, Batista et al. (2011) and Skowron et al. (2011). For the consideration of these higher-order effects, extra parameters must be added in modeling. The parameters for the consideration of the microlens–parallax effects are $(\pi_{\rm E,N}, \pi_{\rm E,E})$, which represent the north and east components of the microlens–parallax vector $\boldsymbol{\pi}_{\rm E} = (\pi_{\rm rel}/\theta_{\rm E})(\boldsymbol{\mu}/\mu)$, respectively. Here, $\pi_{\rm rel} = {\rm AU}(D_{\rm L}^{-1} - D_{\rm S}^{-1})$ represents the relative parallax of the lens and source. Under the approximation of a minor change of the lens configuration by the orbital motion, the lens–orbital effects are described by two parameters $({\rm d}s/{\rm d}t, {\rm d}\alpha/{\rm d}t)$, which represent the change rates of the binary separation and source trajectory angle, respectively.

We analyzed the events by finding lensing solutions, that is, sets of parameters describing the observed light curves. Searches for the lensing parameters were performed in two steps. In the first step, we conducted grid searches for the binary parameters s and q, and for each pair of the grid parameters s and q, we found the other parameters using a downhill approach based on the Markov chain Monte Carlo (MCMC) logic. In this stage, we constructed a χ^2 map on the plane of the grid parameters and identified local solutions on the map. In the second step, we refined the individual local solutions by allowing all parameters to vary. If a single solution can be distinguished from the other local minima with a significant χ^2 difference, we provide a single global solution. If the degeneracy between local solutions is severe, by contrast, we present all local solutions with explanations as to the causes of the degeneracy. In the following subsections, we present the analyses of the individual events.

3.1. KMT-2018-BLG-0321

The source of the lensing event KMT-2018-BLG-0321 lies in the Galactic bulge field with equatorial coordinates $({\rm RA, Dec})_{\rm J2000}$ = (17:41:36.41, −22:09:52.88), which correspond to the Galactic coordinates (l, b) = (5°.301, 4°.315). The event was detected by the KMTNet survey on 2018 July 21 (HJD′ ≡ HJD − 2450000 = 8320.46), when the source was brighter by $\Delta I \sim 1.1$ magnitudes than the baseline of $I_{\rm base} = 18.23$ using the AlertFinder algorithm of the KMTNet survey (Kim et al. 2018b). The source of the event lies in the KMTNet BLG20 field toward which observations were conducted with a 2.5 h cadence.

The lensing light curve of KMT-2018-BLG-0321 presented in Fig. 1 shows that the light curve exhibits deviations from the smooth and symmetric form of a single-lens single-source (1L1S) event. The deviations are characterized by three major anomaly features, including the two spike features appearing around the peak of the light curve at HJD′ ∼ 8352.6 and 8358.2, and the weak bump appearing on the falling side of the light curve at HJD′ ∼ 8373.1. From their shapes, the two spike features are likely to be produced by the source crossing over folds of a binary caustic, and the bump feature is likely to be generated by the source approaching a cusp of the caustic.

From our detailed modeling of the observed light curve, we find that the event was generated by a binary lens with a small mass ratio between the lens components. We find a unique solution without any degeneracy, and the estimated binary parameters are $(s, q) \sim (0.8, 0.1)$. The exact values of the lensing parameters are listed in Table 1 together with the value of χ^2/d.o.f. Neither of the caustic-crossing features is resolved, and only an upper limit on ρ can be constrained. We find that secure measurements of the higher-order lensing parameters

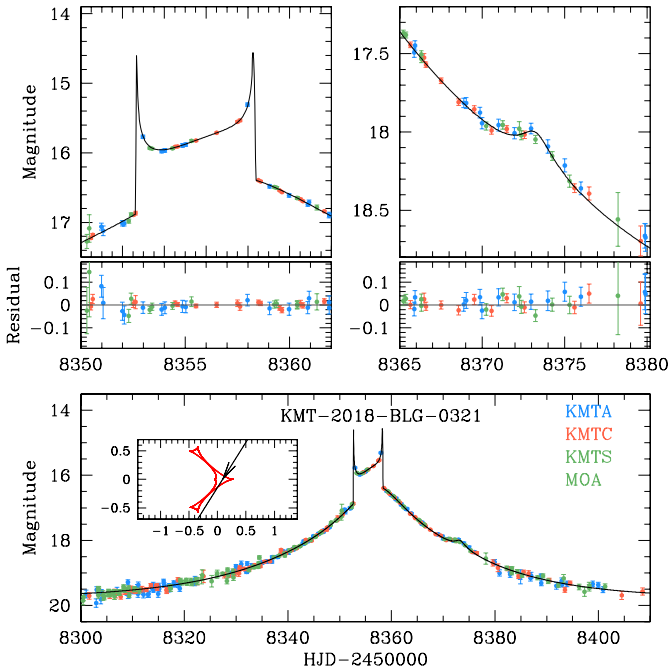

Fig. 1. Light curve of KMT-2018-BLG-0321. The lower panel shows the whole view of the light curve and the two upper panels show the enlarged views of the two anomaly regions. The curve drawn over data points is the best-fit 2L1S model. The inset in the lower panel is the lens system configuration, which shows the source trajectory (line with an arrow) with respect to the lens caustic (red figure). Lengths are normalized to the angular Einstein radius corresponding to the total mass of the lens system.

Table 1. Model parameters of KMT-2018-BLG-0321.

Parameter	Value
χ^2/d.o.f.	721.4/716
t_0 (HJD′)	8355.527 ± 0.019
u_0	0.076 ± 0.001
$t_{\rm E}$ (days)	25.57 ± 0.16
s	0.799 ± 0.002
q	0.103 ± 0.002
α (rad)	5.276 ± 0.005
ρ (10^{-3})	<2.5

Notes. HJD′ = HJD − 2450000.

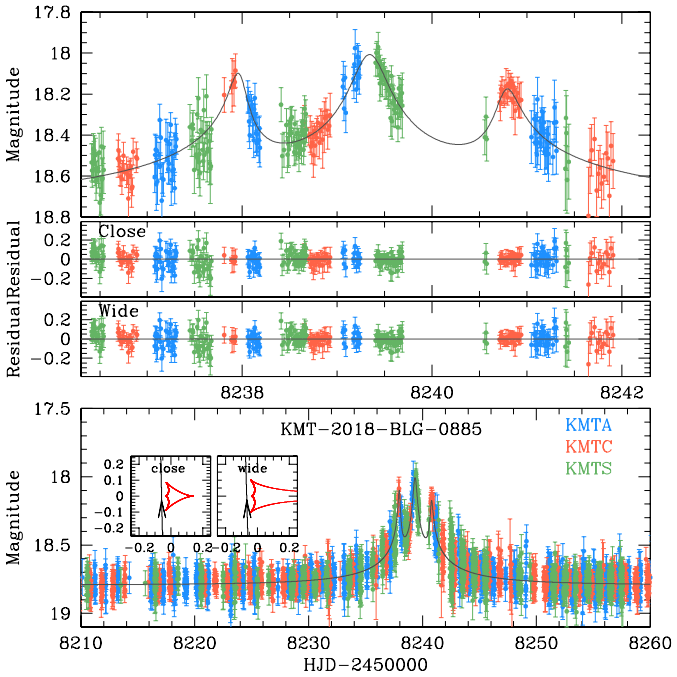

Fig. 2. Light curve of KMT-2018-BLG-0885. Notations are the same as those in Fig. 1. For this event, there exist two degeneration solutions ("close" and "wide" solutions), and two sets of lens system configurations are presented in the bottom panel.

are difficult due to the moderate timescale, $t_{\rm E} \sim 26$ days, of the event.

The inset in the bottom panel of Fig. 1 shows the lens system configuration of the event. The caustic is at the boundary between the close and intermediate regimes, and the two peripheral caustics are connected with the central caustic by slim bridges. The best-fit model indicates that the two caustic spikes were produced when the source entered and exited the central caustic, and the weak bump on the falling side of the light curve was produced when the source approached close to one of the two peripheral caustics.

3.2. KMT-2018-BLG-0885

The lensing event KMT-2018-BLG-0885 occurred on a source lying at (RA, Dec)$_{\rm J2000}$ = (17:55:51.92, −28:30:48.10), (l, b) = (1°.513, −1°.713). The event occurred before the full operation of the KMTNet AlertFinder system, and was identified from an inspection of the data by the KMTNet EventFinder system after the bulge season was over (Kim et al. 2018a). The source of the event lies in the two overlapping KMTNet fields of BLG02 and BLG42, each of which was monitored with a 0.5 h cadence, and thus with a combined cadence of 0.25 h.

The light curve of the event is shown in Fig. 2 and is characterized by three consecutive bumps appearing around the peak with a roughly two-day gap between each consecutive pair of bumps. The deviation pattern of these bumps is smooth, suggesting that they were produced by successive approaches of the source close to three cusps of a caustic. For this event, the low mass ratio between the lens components was expected to some extent, because triple-bump anomalies can be produced when a caustic is skewed and its cusps lie on one side of the caustic; as in, for example, the second microlensing planet, OGLE-2005-BLG-071Lb (Udalski et al. 2005).

Table 2. Model parameters of KMT-2018-BLG-0885.

Parameter	Close	Wide
χ^2/d.o.f.	9735.8/9706	9741.9/9706
t_0 (HJD′)	8239.331 ± 0.012	8239.329 ± 0.014
u_0	0.058 ± 0.004	0.067 ± 0.005
$t_{\rm E}$ (days)	12.14 ± 0.72	11.72 ± 0.75
s	0.618 ± 0.007	1.528 ± 0.027
q	0.096 ± 0.006	0.102 ± 0.007
α (rad)	1.549 ± 0.006	1.543 ± 0.012
ρ (10^{-3})	<10	<10

From detailed modeling of the light curve, we identify two solutions, in which one is in the close binary regime and the other is in the wide binary regime. The binary parameters are $(s, q)_{\rm close} \sim (0.62, 0.096)$ for the close solution and $(s, q)_{\rm wide} \sim (1.53, 0.102)$ for the wide solution. The fact that the binary separations of the close and wide solutions approximately follow the relation $s_{\rm close} \sim 1/s_{\rm wide}$ indicates that the degeneracy between the solutions is caused by the close–wide degeneracy (Griest & Safizadeh 1998; Dominik 1999; An 2005). We present the full lensing parameters of both solutions in Table 2. As expected from the anomaly pattern, the companion-to-primary mass ratio of the lens is small, namely $q \sim 0.1$, suggesting that the companion to the lens is likely to be a BD. It was found that the close solution yields a slightly better fit to the data over the wide solution, but the difference between the fits of the two solutions is small with $\Delta\chi^2 = 6.1$. In Fig. 2, we draw the model curve of the close solution, and present the residuals from the close and wide solutions in the region of the anomalies.

The two insets in the bottom panel of Fig. 2 show the configurations of the close (left inset) and wide (right inset) solutions. Each configuration shows that the three bumps were produced by the source passage close to the three protruding cusps of a caustic generated by a binary lens with a low mass ratio. We were not able to tightly constrain the normalized source radius and were only able to set an upper limit of $\rho_{\rm max} \sim 0.01$.

3.3. KMT-2019-BLG-0297

The source coordinates of the event KMT-2019-BLG-0297 are (RA, Dec)$_{\rm J2000}$ = (18:00:15.19, −28:57:55.01), (l, b) = (1°.602, −2°.772). The source lies in the two overlapping KMTNet prime fields of BLG03 and BLG43, toward which the event was observed with a 0.25 h combined cadence. In the 2019 season, the AlertFinder system was operational, and the event was detected in its early stage on April 5 (HJD′ ∼ 8578.8), when the event was magnified by $\Delta I \sim 1.1$ magnitudes from the baseline of $I_{\rm base} = 19.90$. The event was independently detected by the MOA survey three days after the KMTNet alert.

The lensing light curve of the event constructed with the combination of the KMTNet and MOA data is shown in Fig. 3 and is characterized by a central anomaly that lasted for about two days. The main feature of the anomaly is the sharp spike centered at HJD′ ∼ 8586.9 caused by a caustic crossing. Binary caustics form closed curves, and therefore caustic crossings occur in pairs, that is, when the source enters and exits the caustic. There should therefore be an additional caustic spike, although the data did not cover it. From the curvature of the U-shape pattern after the first caustic spike, it is expected that the second caustic spike occurred at around HJD′ ∼ 8588.5.

Table 3. Model parameters of KMT-2019-BLG-0297.

Parameter	Standard		Higher order
	Close	Wide	(close)
χ^2/d.o.f.	4876.2/4876	5062.2/4876	4791.9/4872
t_0 (HJD′)	8587.370 ± 0.006	8587.593 ± 0.006	8587.413 ± 0.008
u_0	0.0031 ± 0.0003	0.0071 ± 0.0002	0.0042 ± 0.0003
t_E (days)	31.62 ± 0.31	41.36 ± 0.79	35.33 ± 0.77
s	0.563 ± 0.002	2.718 ± 0.021	0.528 ± 0.004
q	0.081 ± 0.002	0.188 ± 0.007	0.086 ± 0.003
α (rad)	2.553 ± 0.005	2.606 ± 0.004	2.568 ± 0.005
ρ (10^{-3})	1.195 ± 0.024	0.837 ± 0.021	1.046 ± 0.029
$\pi_{E,N}$	–	–	0.50 ± 0.72
$\pi_{E,E}$	–	–	−0.29 ± 0.07
ds/dt (yr^{-1})	–	–	−0.87 ± 0.14
$d\alpha/dt$ (yr^{-1})	–	–	−0.61 ± 1.4

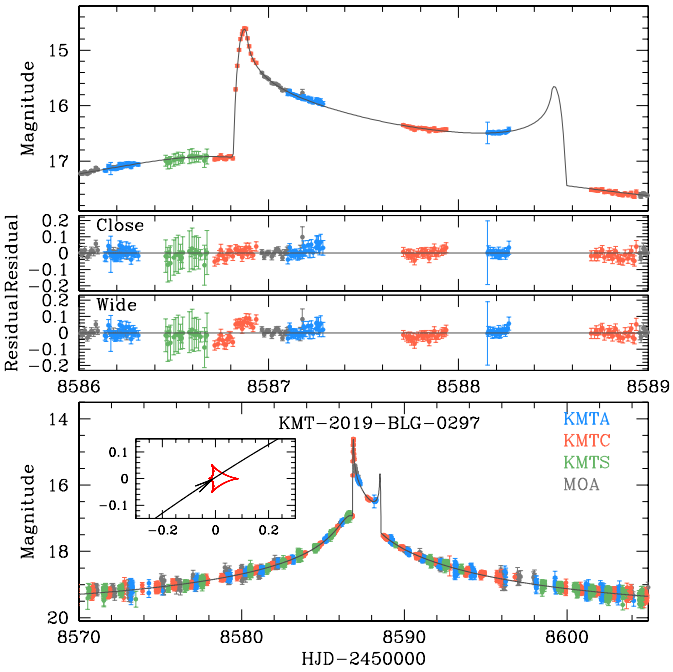

Fig. 3. Light curve of KMT-2019-BLG-0297. Notations are the same as those in Fig. 1. The model curve drawn over the data points is that of the close solution found considering the higher-order effects.

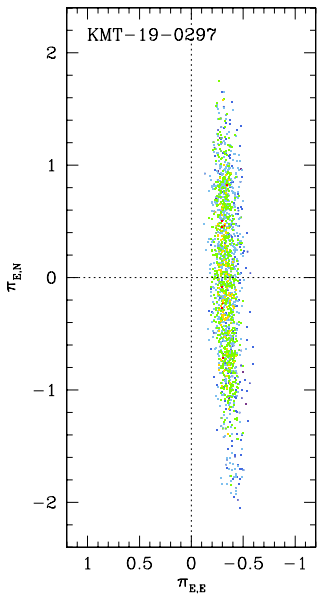

Fig. 4. Scatter plot of MCMC points on the $(\pi_{E,E}, \pi_{E,N})$ plane obtained from modeling the light curve of KMT-2019-BLG-0297 with the consideration of higher-order effects. The color coding represent points with $\leq 1\sigma$ (red), $\leq 2\sigma$ (yellow), $\leq 3\sigma$ (green), $\leq 4\sigma$ (cyan), and $\leq 5\sigma$ (blue).

From our detailed modeling of the light curve, we find that the anomaly in the light curve of the event KMT-2019-BLG-0297 was generated by a close binary ($s \sim 0.56$) with a low mass ratio ($q \sim 0.08$) between the lens components. The full lensing parameters of the solution are presented in Table 3. We find a weak local minimum of a wide binary lens with $(s, q) \sim (2.72, 0.19)$, but its fit is worse than that of the close solution by $\Delta\chi^2 = 186.0$.

With relatively high-precision data in the wings of the light curve, we tested whether the fit further improves with the consideration of higher-order effects. For this check, we conducted an additional modeling, considering both the microlens–parallax and lens–orbital effects. We find that the model considering higher-order effects substantially improves the fit by $\Delta\chi^2 = 84.3$. The lensing parameters of the higher-order solution are listed in Table 3, and the model curve and residual around the anomaly region are shown in Fig. 3. Although turned down, we present the residual of the wide solution for the comparison with the close solution. We note that the variations of the basic lensing parameters with the inclusion of higher-order effects are minor. In Fig. 4, we present the scatter plot of points in the MCMC chain on the $(\pi_{E,N}, \pi_{E,E})$ plane. The plot shows that the east component of the microlens–parallax vector is relatively well constrained, although the north component is not securely measured. As discussed in Sect. 5, the measurement of the microlens parallax is important because π_E provides an extra constraint on the physical parameters of the lens. For KMT-2019-BLG-0297, the angular Einstein radius, which is another observable related to the physical lens parameters, can also be constrained because the caustic entrance was densely resolved by the KMTC data, and this yields the normalized source radius ρ, from which the angular Einstein

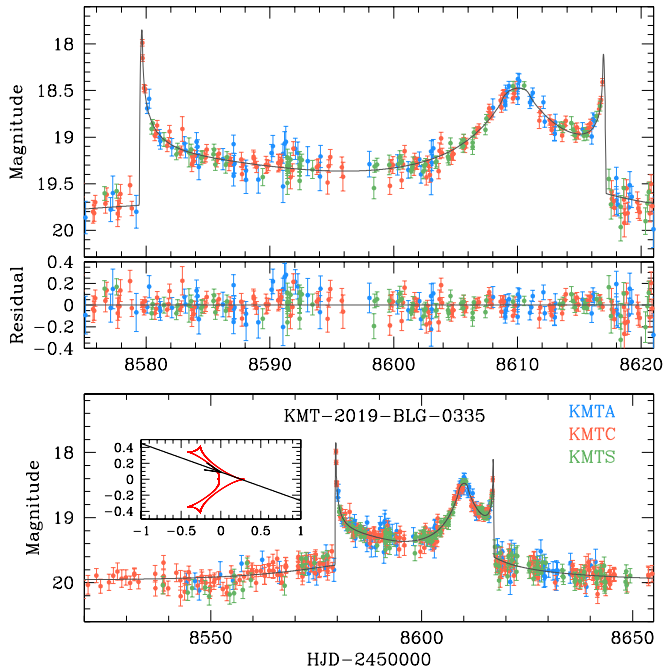

Fig. 5. Light curve of KMT-2019-BLG-0335. Notations are the same as in Fig. 1.

radius is determined as

$$\theta_{\rm E} = \frac{\theta_*}{\rho}. \quad (1)$$

More details about the $\theta_{\rm E}$ determination are discussed in Sect. 4.

3.4. KMT-2019-BLG-0335

The source of the lensing event KMT-2019-BLG-0335 lies at (RA, Dec)$_{\rm J2000}$ = (17:31:21.63, −29:35:26.48), (l, b) = (−2°.215, 2°.279). The source position corresponds to the KMTNet BLG11 field, toward which observations were conducted with a 2.5 h cadence. The lensing magnification of the source flux began before the start of the 2019 observation season, and the event was detected on 2019 April 9 (HJD′ = 8582.6) when the event went through a substantial magnification by the caustic crossing of the source.

Figure 5 shows the lensing light curve of KMT-2019-BLG-0335, which is characterized by three distinctive anomaly features: the two spikes at HJD′ ∼ 8579.0 and 8616.3 and the bump centered at HJD′ ∼ 8610 appearing between the caustic spikes. From the characteristic pattern, the spike features are likely to result from caustic crossings. From the location of the bump appearing in the U-shape region between the caustic-crossing features, it is expected that the bump was produced by the asymptotic approach of the source close to a fold of a caustic as the source proceeded inside the caustic. Although the rising part of the first spike feature and the falling part of the second spike feature were not covered by the data, the pattern of the caustic-crossing features can be well delineated by the data obtained immediately after the first spike and before the second spike.

Detailed modeling of the light curve yields a unique solution with binary parameters of $(s, q) \sim (0.86, 0.064)$, indicating that the anomaly features were produced by a close binary with a low-mass companion. We list the full lensing parameters in Table 4, and the model curve and residual around the anomaly region are presented in Fig. 5. The timescale of the event, $t_{\rm E} \sim 109$ days, is fairly long, but it is difficult to constrain the higher-order lensing parameters due to the substantial photometric errors of the data caused by the faintness of the source. The normalized source radius is measured, although its uncertainty is fairly big because of the incomplete coverage of the caustic crossings.

The inset in the bottom panel of Fig. 5 shows the configuration of the lens system. The caustic is similar to that of KMT-2018-BLG-0321, with the two peripheral caustics connected with the central caustic by narrow bridges, indicating that the binary is at the boundary between the close and intermediate regimes. The source entered the upper left side of the central caustic, passed along its upper right fold, and exited from its lower right side. The caustic entrance and exit produced the spike features, and the bump was generated by the source approach to the caustic fold.

Table 4. Model parameters of KMT-2019-BLG-0335.

Parameter	Value
χ^2/d.o.f.	819.9/823
t_0 (HJD′)	8589.772 ± 0.346
u_0	0.087 ± 0.004
$t_{\rm E}$ (days)	109.22 ± 3.48
s	0.856 ± 0.006
q	0.064 ± 0.004
α (rad)	3.486 ± 0.008
ρ (10^{-3})	0.57 ± 0.15

4. Source stars and Einstein radii

In this section, we specify the source stars of the individual lensing events and estimate angular Einstein radii for the events with measured normalized source radii. For each event, the source is specified by measuring its reddening and extinction-corrected (de-reddened) color and magnitude. The measured source color and magnitude are used to deduce the angular source radius, from which the angular Einstein radius is estimated from the relation in Eq. (1).

Figure 6 shows the source locations of the individual lensing events in the instrumental color–magnitude diagrams (CMDs) of stars lying adjacent to the source stars constructed from pyDIA (Albrow 2017) photometry of the KMTC images. The I- and V-band magnitudes of each source were estimated from the regression of the light-curve data measured using the same pyDIA photometry with respect to the lensing magnification. For the three events KMT-2018-BLG-0321, KMT-2018-BLG-0885, and KMT-2019-BLG-0335, the V-band source magnitudes could not be securely measured due to the poor quality of the V-band data, although their I-band magnitudes were measured. In these cases, we first combine the two sets of CMDs – one constructed from the pyDIA photometry of stars in the KMTC image and the other for stars in the Baade's window observed with the use of the *Hubble* Space Telescope (Holtzman et al. 1998), align the two CMDs using the centroids of the red giant clump (RGC) in the individual CMDs, and then estimate the source color as the median values for stars in the main sequence branch of the HST CMD with I-band magnitude offsets from the RGC centroid corresponding to the measured values. The estimated instrumental colors and magnitudes of the

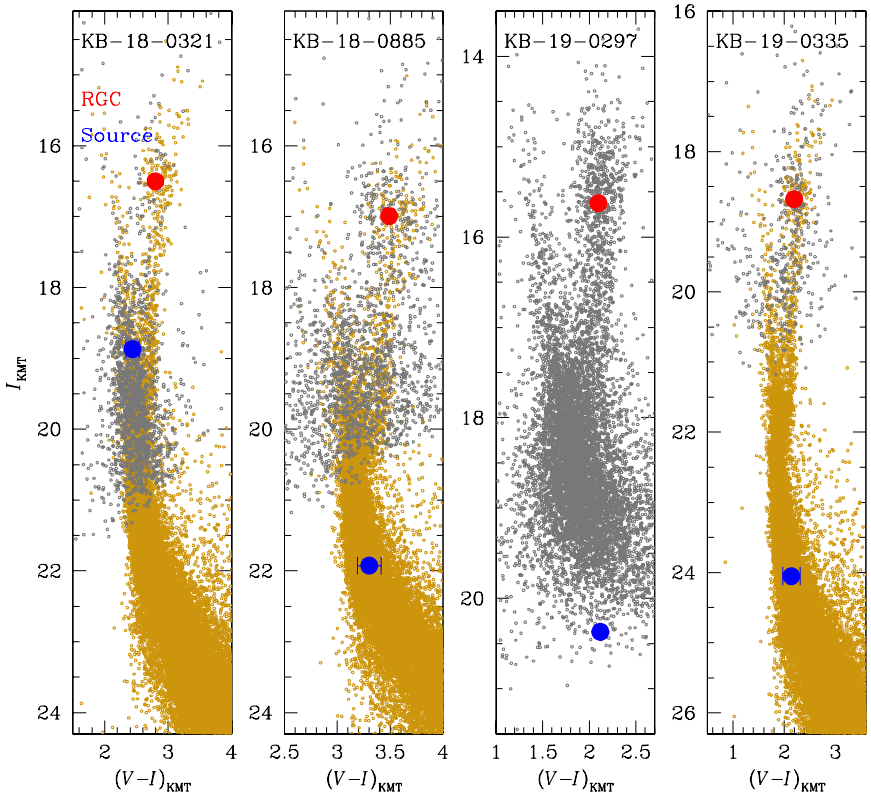

Fig. 6. Source locations (blue filled dots) with respect to the centroids of the RGC (red filled dot) in the CMDs. For the three events KMT-2018-BLG-0321, KMT-2018-BLG-0885, and KMT-2019-BLG-0335, the CMDs are constructed by combining those from KMTC (gray dots) and HST (brown dots) observations.

Table 5. Source properties.

Events	$(V-I, I)_S$	$(V-I, I)_{RGC}$	$I_{0,RGC}$	$(V-I, I)_{0,S}$	θ_* (μas)
KMT-2018-BLG-0321	$(2.441 \pm 0.103, 18.868 \pm 0.029)$	$(2.800, 16.500)$	16.500	$(0.701 \pm 0.103, 16.663 \pm 0.029)$	1.44 ± 0.18
KMT-2018-BLG-0885	$(3.301 \pm 0.112, 21.925 \pm 0.069)$	$(3.490, 16.990)$	14.384	$(0.871 \pm 0.112, 19.319 \pm 0.069)$	0.52 ± 0.07
KMT-2019-BLG-0297	$(2.119 \pm 0.007, 20.371 \pm 0.002)$	$(2.099, 15.624)$	14.382	$(1.079 \pm 0.007, 19.129 \pm 0.002)$	0.71 ± 0.05
KMT-2019-BLG-0335	$(2.139 \pm 0.171, 24.051 \pm 0.028)$	$(2.192, 18.680)$	14.396	$(1.007 \pm 0.171, 19.766 \pm 0.028)$	0.49 ± 0.09

Notes. $(V-I)_{0,RGC} = 1.06$.

source stars, $(V-I, I)_S$, and RGC centroids, $(V-I, I)_{RGC}$, for the individual events are listed in Table 5.

We use the RGC centroid, for which its de-reddened values $(V-I, I)_{0,RGC}$ are well defined (Bensby et al. 2013; Nataf et al. 2013), to calibrate the source colors and magnitudes. By measuring the offsets of the source star from those of the RGC centroid in color and magnitude, $\Delta(V-I, I)$, the de-reddened values are estimated as $(V-I, I)_{0,S} = (V-I, I)_{0,RGC} + \Delta(V-I, I)$. The estimated de-reddened source colors and magnitudes of the individual events are listed in Table 5. According to the estimated de-reddened colors and magnitudes, it is found that the source of KMT-2018-BLG-0321 is a G-type turnoff star, and those of the other events are main sequence stars with spectral types ranging from late G to early K.

The angular radii of the source stars were deduced from their measured colors and magnitudes. For this, we first converted $V-I$ color into $V-K$ color using the Bessell & Brett (1988) relation, and then estimated the angular source radius using the Kervella et al. (2004) relation between $(V-K, I)$ and θ_*. For the events with measured normalized source radii, the angular Einstein radii were estimated using the relation in Eq. (1).

Table 6. Einstein radius and proper motion.

Event	θ_E (mas)	μ (mas yr^{-1})
KMT-2018-BLG-0321	>0.57	>2.4
KMT-2018-BLG-0885	>0.05	>1.6
KMT-2019-BLG-0297	0.60 ± 0.04	6.93 ± 0.51
KMT-2019-BLG-0335	0.19 ± 0.07	2.87 ± 1.16

The estimated angular radii of the source stars and Einstein rings of the individual events are listed in Table 6. Also listed are the relative proper motions between the lens and source estimated by $\mu = \theta_E/t_E$. In the cases of the events KMT-2018-BLG-0321 and KMT-2018-BLG-0885, for which only the upper limits of ρ are constrained, we list the lower limits of θ_E and μ.

5. Physical lens properties

The basic lensing observable constraining the physical parameters of the lens mass M and distance to the lens D_L is the Einstein

Table 7. Physical lens parameters.

Events	M_1 ($M_\odot$)	M_2 ($M_\odot$)	D_L (kpc)	$a_\perp$ (AU)
KMT-2018-BLG-0321	$0.75^{+0.33}_{-0.29}$	$0.072^{+0.042}_{-0.038}$	$4.23^{+1.15}_{-1.57}$	$2.54^{+0.69}_{-0.95}$
KMT-2018-BLG-0885 (close)	$0.29^{+0.38}_{-0.18}$	$0.028^{+0.037}_{-0.018}$	$6.89^{+1.06}_{-1.24}$	$1.07^{+0.17}_{-0.19}$
(wide)	–	$0.030^{+0.039}_{-0.019}$	–	$2.64^{+0.41}_{-0.47}$
KMT-2019-BLG-0297	$0.21^{+0.09}_{-0.07}$	$0.018^{+0.008}_{-0.007}$	$3.09^{+0.76}_{-0.68}$	$0.96^{+0.24}_{-0.21}$
KMT-2019-BLG-0335	$0.32^{+0.35}_{-0.19}$	$0.020^{+0.022}_{-0.012}$	$7.71^{+0.99}_{-1.22}$	$1.64^{+0.21}_{-0.26}$

timescale t_E, which is related to the physical parameters by

$$t_E = \frac{\theta_E}{\mu}; \qquad \theta_E = (\kappa M \pi_{rel})^{1/2}, \tag{2}$$

where $\kappa = 4G/(c^2 \mathrm{AU})$. In addition to this observable, the lens mass and distance can also be constrained by measuring the extra observables of π_E and θ_E. If both of these extra observables are simultaneously measured, the physical lens parameters can be uniquely determined by the relation

$$M = \frac{\theta_E}{\kappa \pi_E}; \qquad D_L = \frac{\mathrm{AU}}{\pi_E \theta_E + \pi_S}, \tag{3}$$

where $\pi_S = \mathrm{AU}/D_S$ is the parallax of the source, and D_S denotes the distance to the source (Gould 2000). For KMT-2019-BLG-0297, both of these extra parameters are measured, but the uncertainty of the measured microlens parallax is large. For the event KMT-2019-BLG-0335, the Einstein radius is measured, but the values of π_E are not constrained. For the KMT-2018-BLG-0321 and KMT-2018-BLG-0885, none of the extra observables are measured, and only the lower limits on θ_E are constrained. Due to the incompleteness of the observables, we estimated the physical lens parameters by conducting Bayesian analyses based on the available observables of the individual events.

The Bayesian analysis for each event was carried out by first generating a large number (10^7) of artificial microlensing events from a Monte Carlo simulation with the use of a prior Galactic model. The Galactic model defines the positions, velocities, and masses of astronomical objects in the Galaxy, and we adopted the Jung et al. (2021) model. For each simulated event, we computed the lens observables of the Einstein timescale, $t_{E,i} = D_{L,i}\theta_{E,i}/v_{\perp,i}$, Einstein radius, $\theta_{E,i} = (\kappa M_i \pi_{rel,i})^{1/2}$, and microlens parallax, $\pi_{E,i} = \pi_{rel,i}/\theta_{E,i}$. Here, $v_\perp$ denotes the transverse lens–source speed. We then constructed Bayesian posterior distributions of the lens mass and distance by imposing a weight to each simulated event of $w_i = \exp(-\chi_i^2/2)$, where $\chi_i^2 = (O_i - O)^2/[\sigma(O)]^2$ and $[O, \sigma(O)]$ denote the measured value of the observable and its uncertainty, respectively. In the case of the event for which only the lower limit of θ_E is constrained, we set $w_i = 0$ for events with $\theta_E < \theta_{E,\min}$.

The posterior distributions for the mass of the lens companion and distance to the lens system are presented in Figs. 7 and 8, respectively. In each distribution, we mark three curves, in which the blue and red curves represent the contributions from the disk and bulge lens populations, respectively, and the black curve is the sum of the two contributions. The two vertical lines in the mass posteriors represent the boundaries between planetary, BD, and stellar lens populations. We set the boundary between planets and BDs as 12 M_J ($M_2 \sim 0.012\ M_\odot$) and that between BDs and stars as 0.08 $M_\odot$.

In Table 7, we summarize the estimated physical lens parameters, including M_1, M_2, D_L, and $a_\perp$, where $a_\perp = sD_L\theta_E$ denotes

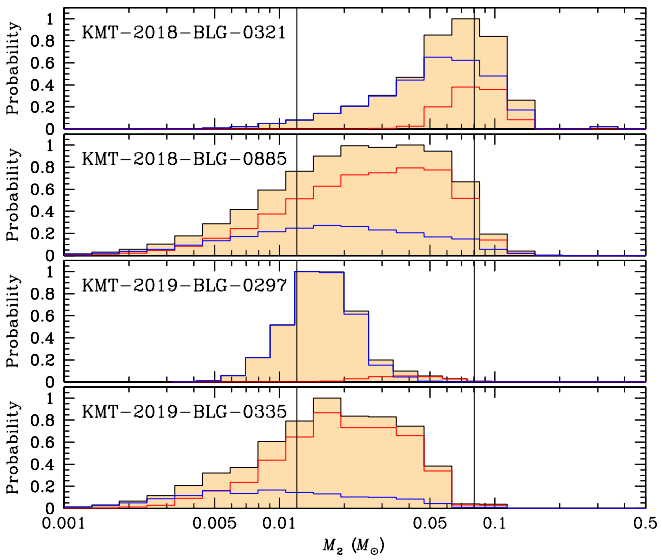

Fig. 7. Bayesian posteriors for the masses of the lens companions. The blue and red curves in each panel indicate the contributions from the disk and bulge lens populations, respectively, and the black curve is the sum of the contributions. The two vertical lines at $M_2 = 0.012\ M_\odot$ (∼12 M_J) and 0.08 $M_\odot$ indicate the boundaries between planetary, BD, and stellar lens populations.

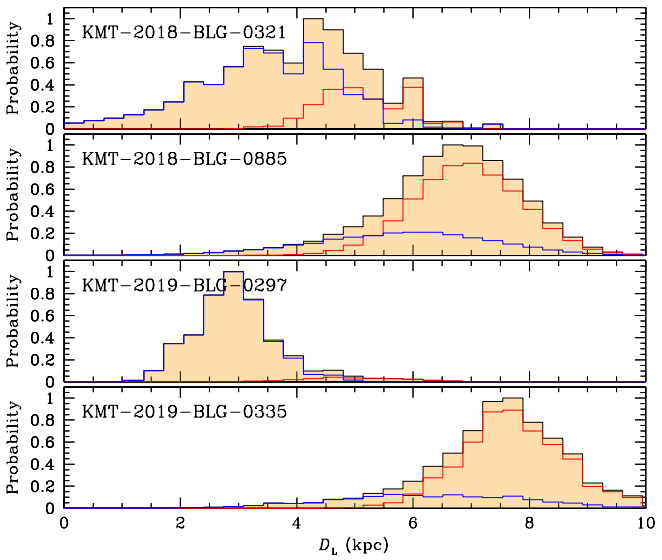

Fig. 8. Bayesian posteriors for the distances of the lens systems. Notations are the same as those in Fig. 7.

Table 8. Probabilities of the lens population and location.

Events	$P_{\rm BD}$	$P_{\rm planet}$	$P_{\rm star}$	$P_{\rm disk}$	$P_{\rm bulge}$
KMT-2018-BLG-0321	59	3	38	75	25
KMT-2018-BLG-0885	68	25	7	29	71
KMT-2019-BLG-0297	66	34	0	94	6
KMT-2019-BLG-0335	66	33	10	22	78

the projected separation between the binary lens components. We take the median values of the posterior distributions as representative values, and the uncertainties are estimated as the 16% and 84% of the distributions. In Table 8, we list the probabilities for the lens companion to be in the planetary ($P_{\rm planet}$), BD ($P_{\rm BD}$), and stellar ($P_{\rm star}$) mass regimes. In all cases of the events, the median values of M_2 lie in the BD mass regime, and the probabilities for the lens companion to be in the BD mass regime are high. For the events KMT-2018-BLG-0885, KMT-2019-BLG-0297, and KMT-2019-BLG-0335, the probabilities for the lens companions to be in the planetary mass regime are $P_{\rm planet} \sim 25\%$, 34%, and 33%, respectively, and therefore it is difficult to completely rule out the possibility that the companions are giant planets. Also listed in Table 8 are the probabilities for the lens to be in the disk, $P_{\rm disk}$, and in the bulge, $P_{\rm bulge}$. We find KMT-2019-BLG-0297L to very likely be in the disk mainly from the two-dimensional Gaussian constraint of the measured microlens parallax; see Fig. 4.

6. Summary and conclusion

We investigated the microlensing data acquired during the 2018, 2019, and 2020 seasons of the KMTNet survey in order to find lensing events produced by binaries with BD companions. For this investigation, we conducted systematic analyses of anomalous lensing events observed during the seasons, and picked out candidate BD binary-lens events by applying the selection criterion that the companion-to-primary mass ratio be less than 0.1. From this procedure, we identified four candidate events with BD companions, including KMT-2018-BLG-0321, KMT-2018-BLG-0885, KMT-2019-BLG-0297, and KMT-2019-BLG-0335. No candidates were identified in the 2020 season, which was severely affected by the Covid-19 pandemic.

We estimated the masses of the lens companions by conducting Bayesian analyses using the measured observables of the individual events. From this estimation, we find that the probabilities for the masses of the companions to be in the BD mass regime are high, with 59%, 68%, 66%, and 66% for KMT-2018-BLG-0321, KMT-2018-BLG-0885, KMT-2019-BLG-0297, and KMT-2019-BLG-0335, respectively. We plan to report additional BD binary-lens events from investigation of the data acquired in the 2021 and 2022 seasons. Together with the previous six BD events (OGLE-2016-BLG-0890, MOA-2017-BLG-477, OGLE-2017-BLG-0614, KMT-2018-BLG-0357, OGLE-2018-BLG-1489, and OGLE-2018-BLG-0360) reported in Paper I, plus KMT-2020-BLG-0414LB recently reported by Zang et al. (2021), the KMTNet sample will be useful for a future statistical analysis of the properties of BDs.

Acknowledgements. Work by C.H. was supported by the grants of National Research Foundation of Korea (2019R1A2C2085965). This research has made use of the KMTNet system operated by the Korea Astronomy and Space Science Institute (KASI) at three host sites of CTIO in Chile, SAAO in South Africa, and SSO in Australia. Data transfer from the host site to KASI was supported by the Korea Research Environment Open NETwork (KREONET). The MOA project is supported by JSPS KAKENHI Grant Number JSPS24253004, JSPS26247023, JSPS23340064, JSPS15H00781, JP16H06287, and JP17H02871. J.C.Y. acknowledges support from NSF Grant No. AST-2108414. Y.S. acknowledges support from NSF Grant No. 2020740. W.Z. and H.Y. acknowledges support by the National Science Foundation of China (Grant No. 12133005). C.R. was supported by the Research fellowship of the Alexander von Humboldt Foundation.

References

Albrow, M., Horne, K., Bramich, D. M., et al. 2009, MNRAS, 397, 2099
Albrow, M. 2017, https://doi.org/10.5281/zenodo.268049
An, J. H. 2005, MNRAS, 356, 1409
Batista, V., Gould, A., Dieters, S. et al. 2011, A&A, 529, A102
Bensby, T. Yee, J.C., Feltzing, S. et al. 2013, A&A, 549, A147
Bessell, M. S., & Brett, J. M. 1988, PASP, 100, 1134
Bond, I. A., Abe, F., Dodd, R. J., et al. 2001, MNRAS, 327, 868
Cassan, A. 2008, A&A, 491, 587
Dominik, M. 1999, A&A, 349, 108
Gould, A. 1992, ApJ, 392, 442
Gould, A. 2000, ApJ, 542, 785
Gould, A. 2022, arXiv e-print [arXiv:2209.12501]
Gould, A., & Loeb, A. 1992, ApJ, 396, 104
Gould, A., Han, C., Weicheng, Z., et al. 2022, A&A, 664, A13
Grether, D., & Lineweaver, C. H. 2006, ApJ, 640, 1051
Griest, K., & Safizadeh, N. 1998, ApJ, 500, 37
Han, C., & Gould, A. 2003, ApJ, 592, 172
Han, C., Lee, C.-U., Udalski, A., et al. 2020, AJ, 159, 134
Han, C., Ryu, Y.-H., Shin, I.-G., et al. 2022, A&A, 667, A64
Holtzman, J. A., Watson, A. M., Baum, W. A., et al. 1998, AJ, 115, 1946
Jung, Y. K., Han, C., Udalski, A., et al. 2021, AJ, 161, 293
Jung, Y. K., Zang, W., Han, C., et al. 2022, AJ, 164, 262
Kervella, P., Thévenin, F., Di Folco, E., & Ségransan, D. 2004, A&A, 426, 29
Kim, S.-L., Lee, C.-U., Park, B.-G., et al. 2016, JKAS, 49, 37
Kim, D.-J., Kim, H.-W., Hwang, K.-H., et al., 2018a, AJ, 155, 76
Kim, H.-W., Hwang, K.-H., Shvartzvald, Y., et al. 2018b, arXiv e-prints [arXiv:1806.07545]
Nataf, D. M., Gould, A., Fouqué, P. et al. 2013, ApJ, 769, 88
Shvartzvald, Y., Maoz, D., Udalski, A., et al. 2016, MNRAS, 457, 4089
Shvartzvald, Y., Yee, J. C., Skowron, J., et al. 2019, AJ, 157, 106
Skowron, J., Udalski, A., Gould, A., et al. 2011, ApJ, 738, 87
Schneider, P., & Weiss, A. 1986, A&A, 164, 237
Tsapras, Y., Street, R. A., Hundertmark, M., et al. 2019, PASP, 131, 124401
Udalski, A., Jaroszyński, M., Paczyński, B, et al. 2005, ApJ, 628, L109
Udalski, A., Szymański, M. K., & Szymański, G. 2015, Acta Astron., 65, 1
Whitworth, A., Bate, M. R., Nordlund, A. A., Reipurth, B., & Zinnecker, H. 2007, in Protostars and Planets, 951 eds. V. B. Reipurth, D. Jewitt, & K. Keil (Tucson: University Arizona Press), 459
Yee, J. C., Shvartzvald, Y., Gal-Yam, A., et al. 2012, ApJ, 755, 102
Yoo, J., DePoy, D.L., Gal-Yam, A. et al. 2004, ApJ, 603, 139
Zang, W., Han, C., Kondo, I., et al. 2021, Res. Astron. Astrophys., 21, 239

[1] Department of Physics, Chungbuk National University, Cheongju 28644, Republic of Korea
e-mail: cheongho@astroph.chungbuk.ac.kr
[2] Korea Astronomy and Space Science Institute, Daejon 34055, Republic of Korea
[3] Max-Planck-Institute for Astronomy, Königstuhl 17, 69117 Heidelberg, Germany
[4] Department of Astronomy, Ohio State University, 140 W. 18th Ave., Columbus, OH 43210, USA
[5] Dipartimento di Fisica "E. R. Caianiello", Universitá di Salerno, Via Giovanni Paolo II, 84084 Fisciano (SA), Italy
[6] Istituto Nazionale di Fisica Nucleare, Sezione di Napoli, Via Cintia, 80126 Napoli, Italy
[7] Institute of Natural and Mathematical Science, Massey University, Auckland 0745, New Zealand
[8] University of Canterbury, Department of Physics and Astronomy, Private Bag 4800, Christchurch 8020, New Zealand
[9] Center for Astrophysics, Harvard & Smithsonian, 60 Garden St., Cambridge, MA 02138, USA

[10] Department of Particle Physics and Astrophysics, Weizmann Institute of Science, Rehovot 76100, Israel
[11] Department of Astronomy, Tsinghua University, Beijing 100084, PR China
[12] School of Space Research, Kyung Hee University, Yongin, Kyeonggi 17104, Republic of Korea
[13] Korea University of Science and Technology, Korea, (UST), 217 Gajeong-ro, Yuseong-gu, Daejeon 34113, Republic of Korea
[14] Institute for Space-Earth Environmental Research, Nagoya University, Nagoya 464-8601, Japan
[15] Code 667, NASA Goddard Space Flight Center, Greenbelt, MD 20771, USA
[16] Department of Astronomy, University of Maryland, College Park, MD 20742, USA
[17] Department of Earth and Planetary Science, Graduate School of Science, The University of Tokyo, 7-3-1 Hongo, Bunkyo-ku, Tokyo 113-0033, Japan
[18] Instituto de Astrofísica de Canarias, Vía Láctea s/n, 38205 La Laguna, Tenerife, Spain
[19] Department of Earth and Space Science, Graduate School of Science, Osaka University, Toyonaka, Osaka 560-0043, Japan
[20] Department of Physics, The Catholic University of America, Washington, DC 20064, USA
[21] Department of Astronomy, Graduate School of Science, The University of Tokyo, 7-3-1 Hongo, Bunkyo-ku, Tokyo 113-0033, Japan
[22] Zentrum für Astronomie der Universität Heidelberg, Astronomisches Rechen-Institut, Mönchhofstr. 12–14, 69120 Heidelberg, Germany
[23] Department of Physics, University of Auckland, Private Bag 92019, Auckland, New Zealand
[24] University of Canterbury Mt. John Observatory, PO Box 56, Lake Tekapo 8770, New Zealand